## PAPER

Check for updates

# Solar-light-triggered regenerative adsorption removal of styrene by silver nanoparticles incorporated in metal–organic frameworks†

Hongli Liu,[ab] Mingjie Xu,[ab] Guiying Li, [iD] [ab] Weiping Zhang[ab] and Taicheng An [iD] *[ab]

Adsorption is an attractive technique for the removal of volatile organic compounds (VOCs) from polluted air; however, it is still challenging to efficiently release adsorbed VOCs. Herein, in consideration of the unprecedented VOC adsorption capability of MOFs and excellent photothermal effects of Ag nanoparticles, a novel photodynamic Ag/UiO-66 adsorbent was constructed by integrating Ag nanoparticles with UiO-66 using a colloidal deposition method. The obtained Ag/UiO-66 samples were found to possess the excellent porosity and high styrene adsorption capability of parent UiO-66. Upon exposure to simulated solar light, Ag nanoparticles could convert light energy into thermal energy, which gave rise to light-induced localized heat near Ag nanoparticles. Subsequently, this localized heat triggered the thermal desorption of the adsorbed styrene from Ag/UiO-66, thus successfully realizing efficient *in situ* regeneration of Ag/UiO-66 under solar light irradiation. Moreover, the desorption capacity can be effectively regulated by the Ag content. More importantly, the regenerability of Ag/UiO-66 remained intact even after five adsorption–desorption cycles; however, pure UiO-66 recovered only 51.6% of its adsorption capacity and maintained 77.0% of its desorption capacity after five cycles. Furthermore, adsorption kinetic parameters and a possible regeneration mechanism are described in detail.

### Environmental significance

Adsorption is an attractive technique for the removal of volatile organic compounds from polluted air; however, it remains challenging due to the great energy penalty associated with regeneration of adsorbents. Therefore, a novel photodynamic Ag/UiO-66 adsorbent was constructed by the integration of high VOCs adsorption capability of MOF and the excellent photothermal effects of Ag nanoparticles, and its *in situ* regeneration was realized under solar light irradiation by light-induced localized heat. Importantly, no appreciable decline was observed in both the adsorption and desorption efficiencies of Ag/UiO-66 after five adsorption–desorption cycles. Considering the exceptional adsorption properties and green *in situ* regeneration process triggered by naturally abundant solar light, the development of photothermal MOF-based composites may open new avenues for adsorption applications.

## 1. Introduction

Volatile organic compounds (VOCs) are among most crucial air contaminants; they mainly originate from diverse chemical process industries, including petrochemicals, polymer syntheses, paint and coatings.[1] Due to the severe biological toxicity and photochemical behaviours of VOCs even at very low concentrations,[2,3] the development of environmentally benign methods for efficient removal of gaseous VOCs from polluted air has received considerable attention, and multiple techniques have been screened to control VOC emissions, such as absorption, adsorption, catalytic oxidation and biofiltration.[1,4–12] Among these methods, the adsorption technique has been intensively investigated because it is economic, highly efficient, and also holds great potential to recover both valuable VOCs and adsorbents for further reuse. Some porous materials (*e.g.*, activated carbon, polymeric resins, zeolite) which possess high specific surface areas and pore volumes are commonly used as adsorbents.[7–12] However, their limited adsorption capability and difficulties in regeneration have restricted their applications in the removal of VOCs.[10,11] In particular, regeneration is a great concern for the practical application

[a] *Guangdong Key Laboratory of Environmental Catalysis and Health Risk Control, Guangdong-Hong Kong-Macao Joint Laboratory for Contaminants Exposure and Health, Institute of Environmental Health and Pollution control, Guangdong University of Technology, Guangzhou 510006, China. E-mail: antc99@gdut.edu.cn*
[b] *Guangzhou Key Laboratory of Environmental Catalysis and Pollution Control, Key Laboratory of City Cluster Environmental Safety and Green Development, School of Environmental Science and Engineering, Guangdong University of Technology, Guangzhou 510006, China*
† Electronic supplementary information (ESI) available: XRD data, TEM images, FT-IR spectra, *in situ* DRIFTS spectra, acidity, as well as additional adsorption and desorption results. See DOI: 10.1039/d0en01011a

This journal is © The Royal Society of Chemistry 2021

*Environ. Sci.: Nano*, 2021, **8**, 543–553 | **543**

of adsorbents. Currently, heating, vacuum and hot gas purging are often implemented to release VOCs and regenerate adsorbents.[9–12] Apparently, these regeneration approaches usually involve high energy consumption and potential changes in the properties of adsorbents.[11] Therefore, the development of advanced adsorbents in combination with efficient regeneration approaches, which can offer high adsorption capability and excellent regenerability, is extremely imperative.

In addition to high pore volume and specific surface area, metal–organic frameworks (MOFs) as an emerging class of porous materials possess many unique characteristics, including open and ordered pore structures, abundant interconnected 3D channels, ultrahigh porosity, and tailorable chemical properties.[13–16] These distinguished features endow MOFs with great potential toward application as adsorbents in the removal of VOCs.[14–16] Accordingly, MOFs have been extensively investigated and proved to exhibit significant improvements in terms of their adsorption capacities compared with traditional porous adsorbents.[15–21] For instance, hybrid MIL-101(Cr)@PFs composites synthesized via loading MIL-101(Cr) onto pulp fibers have been used for the adsorption of benzene vapor.[15] Moreover, MIL-101(Cr)@PFs with an MIL-101(Cr) content of 67% displayed an optimal benzene equilibrium uptake of 10.29 mmol g$^{-1}$, which is 12, 10 and 7.7 times as high as those of SBA-15, silicalite-1, and H-ZSM-5, respectively. Shafiei et al. reported that a modified M-MIL-101(Cr) exhibited extraordinarily high adsorption capacity for six investigated VOCs,[21] with approximately 3.6–7.4 times more capacity than commercially activated carbons. Unfortunately, the regeneration of the MOF adsorbents was still implemented by conventional gas liberating strategies.

On the other hand, surface plasmon resonance (SPR) of metallic nanostructures has aroused much interest due to its ability to convert incident light into thermal energy, therefore opening up numerous opportunities for various applications from artificial actuators to solar steam generation, sensors, photocatalysis and cancer photothermal therapy.[22–27] Particularly, for drug delivery applications, it has been demonstrated that the localized heating generated by metallic nanostructures under light irradiation can efficiently trigger the release of loaded molecules.[26,27] Considering the outstanding VOCs adsorption capacity of MOFs and the light-induced local heating of metallic nanostructures, we speculate that it would be a feasible strategy for VOCs adsorption and subsequent light-induced regeneration via integrating the advantages of both MOFs and metal nanoparticles with SPR.

Herein, as a proof-of-concept, we report the construction of Ag/UiO-66 nanocomposites by incorporation of Ag nanoparticles into UiO-66 using a colloidal deposition method, and their potential application in VOC adsorption and light-induced regeneration are also attempted. In this combination, the abundant interconnected and open 3D cavities within MOFs would allow the facile diffusion of VOCs
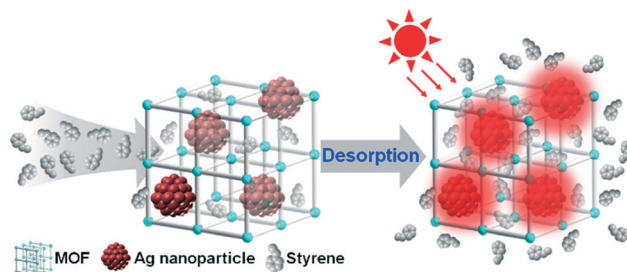


Scheme 1 Illustration of the solar-light-triggered styrene adsorption/desorption process using Ag/UiO-66 as an adsorbent.

and the facile penetration of light. Moreover, the localized heat generated by metal nanoparticles would promote the fast desorption of their surrounding VOCs, thus avoiding heating of the entire adsorbent bed (Scheme 1). As expected, the Ag/UiO-66 samples exhibited typical SPR absorption of Ag nanoparticles, and the SPR absorption intensity was effectively regulated by the Ag content. Evidently, the surface temperature of the Ag/UiO-66 samples was found to be remarkably enhanced within minutes after exposure to simulated solar light. We further examined the application of the Ag/UiO-66 nanocomposites in the in situ adsorption–desorption of VOCs for air purification under solar irradiation. Finally, a possible regeneration mechanism for the photo-induced desorption of VOCs over the Ag/UiO-66 nanocomposites was also proposed.

## 2. Experimental section

### 2.1 Chemicals

All chemical reagents were purchased commercially and employed without further modification. Zirconium tetrachloride (ZrCl$_4$, 98%) and terephthalic acid (98%) were purchased from J&K Scientific Ltd. Ethanol (A.R.), methanol (A.R.), acetic acid (A.R.) and N,N-dimethylformamide (DMF, A.R.) were obtained from Guangzhou Jinhuada Chemical Reagent Co., Ltd. Silver nitrate (AgNO$_3$, A.R.), sodium borohydride (NaBH$_4$, A.R.), polyvinylpyrrolidone (PVP, M.W. = 56 000) and styrene were obtained from Shanghai Aladdin Reagent Co., Ltd.

### 2.2 Materials synthesis

**Synthesis of UiO-66.** UiO-66 was synthesized according to a reported procedure in the literature with a few modifications.[28] In a typical synthesis, 133.6 mg of ZrCl$_4$, 100 mg of terephthalic acid, 4 mL of glacial acetic acid and 40 mL of DMF were added to a 100 mL Schlenk tube. Subsequently, the uniform mixture was obtained by ultrasonication for 30 min and then underwent hydrothermal reaction at 130 °C for 24 h. After cooling to room temperature, the generated white powder sample was washed with DMF and methanol several times. Finally, the activated sample was achieved under dynamic vacuum at 130 °C for 12 h.

544 | Environ. Sci.: Nano, 2021, 8, 543–553

This journal is © The Royal Society of Chemistry 2021

**Synthesis of Ag/UiO-66 nanocomposites.** UiO-66-Supported silver nanoparticles were synthesized using a simple colloidal deposition method. Typically, the required amount of PVP (PVP monomer/Ag = 15 : 1, molar ratio) was dispersed in an AgNO₃ methanol solution under vigorous stirring. Subsequently, a fresh methanol solution of NaBH₄ (0.1 M, NaBH₄/Ag = 5 : 1, molar ratio) was quickly added to the above mixture. Then, the activated UiO-66 was added, and the formed suspension was further stirred for 10 h. The solid was collected, washed with methanol, and finally dried under vacuum at 100 °C for 12 h to obtain the Ag/UiO-66 samples.

## 2.3 Characterization

The crystal structures of the synthesized samples were obtained by powder X-ray diffraction (D/MAX-Ultima IV, Cu Kα radiation, 40 kV, 40 mA) with a scan rate of 6° min⁻¹. Fourier transform-infrared spectra (FT-IR) were recorded on a Nicolet iS10 instrument in the range of 500–4000 cm⁻¹ using the KBr pellet technique. The loading of Ag in the Ag/UiO-66 nanocomposites was analysed *via* flame atomic absorption spectroscopy. The specific surface areas and pore structures were measured using a Micromeritics ASAP 2020 by the low temperature N₂ adsorption–desorption method. UV-vis diffuse reflectance spectra were collected by an Agilent Cary 300 spectrophotometer using BaSO₄ as a standard reference. A transmission electron microscope (JEM-2010HR, Japan) with EDX analysis (Oxford INCA EDS) was employed to observe the morphologies and structures of the samples. A thermal imaging infrared camera (Fluke, TiX640) was employed to monitor the temperature changes of the UiO-66 and Ag/UiO-66 samples under the illumination of a 300 W xenon lamp.

The surface acidity of the samples was investigated by a Nicolet iS10 Fourier transform infrared spectrometer employing pyridine as a probe molecule. The solid sample was firstly pressed into a self-supporting thin slice and then was *in situ* degassed in a quartz infrared chamber at 200 °C in a vacuum of 10⁻² Pa for 2 h. After the sample was cooled to room temperature, the pyridine vapor was introduced into the sample chamber and equilibrated for 30 min. Subsequently, the excess pyridine on the surface of the sample was removed at 40 °C for 1 h under vacuum. Finally, the FTIR spectrum was collected at 30 °C after heating the sample at 250 °C for 1 h.

The surface acidities of Brønsted acid and Lewis acid were calculated based on the molar extinction coefficients previously reported in the literature.[29] The formulas were as follows (eqn (1) and (2), respectively):

$$C_B = 1.88 \frac{IA(B)R^2}{W} \tag{1}$$

$$C_L = 1.42 \frac{IA(L)R^2}{W} \tag{2}$$

where $C_B$ and $C_L$ refer to the concentrations of the Brønsted acid and Lewis acid, respectively, in mmol g⁻¹ catalyst; IA(B) refers to the integrated absorbance of the Brønsted band

(cm⁻¹); IA(L) refers to the integrated absorbance of the Lewis acid (cm⁻¹); $R$ refers to the radius of the sample slice (cm); and $W$ refers to the weight of the sample slice (mg).

## 2.4 Adsorption and desorption performance measurements

The adsorption experiments were carried out in a fixed-bed quartz reactor under ambient pressure in the dark. Typically, 0.1 g of the adsorbent was filled into the reactor and pretreated in N₂ at 120 °C for 4 h to remove the adsorbed impurities. After cooling to 30 °C, the inlet gas was switched from N₂ to a gas mixture with a styrene concentration of 200 ± 1 ppmv balanced by air at a stable flow rate of 25 mL min⁻¹ by mass flow controllers to start the adsorption test. The styrene concentration of the outlet gas was continuously monitored by an online gas chromatograph with a flame ionization detector.

After the establishment of the gas–solid adsorption equilibrium, the inlet gas was switched to N₂ with a flow rate of 25 mL min⁻¹. Meanwhile, a 300 W Xe lamp with a wavelength range of 320–780 nm that was vertically placed above the reactor with a distance of 12 cm was turned on to investigate the desorption behaviours. The composition of the effluent gas, including styrene and the possible organic products as well as mineralization products, was detected using an online gas chromatograph with two flame ionization detectors.

Based on the breakthrough curve, the adsorption capacity ($q$, mg g⁻¹) of the adsorbent was calculated using eqn (3):

$$q = \frac{V}{1000\,m}\left(C_0 t - \int_0^t C_t \mathrm{d}t\right) \tag{3}$$

The desorption capacity of the adsorbent was calculated on the basis of the desorption curve using eqn (4):

$$q = \frac{V}{1000\,m}\int_0^t C_t \mathrm{d}t \tag{4}$$

where $C_0$ and $C_t$ (mg L⁻¹) represent the concentrations of styrene at the inlet and outlet, respectively; $V$ is the volumetric flow rate (mL min⁻¹) of the gaseous styrene; $m$ (g) is the mass of adsorbers in the reactor; and $t$ (min) represents the adsorption time.

The adsorption kinetics of styrene on the adsorbents were obtained by fitting the experimental adsorption data using pseudo-first order and pseudo-second order models, respectively. The pseudo-first order and pseudo-second order models are expressed as eqn (5) and (6), respectively:

$$q_t = q_e(1 - \exp(-k_f t)) \tag{5}$$

$$q_t = \frac{q_e^2 k_s t}{1 + q_e k_s t} \tag{6}$$

where $q_t$ (mg g⁻¹) represents the styrene adsorption amount at any adsorption time $t$ (min), $q_e$ (mg g⁻¹) represents the equilibrium adsorption capacity of styrene, and $k_f$ (min⁻¹)

This journal is © The Royal Society of Chemistry 2021

*Environ. Sci.: Nano*, 2021, **8**, 543–553 | **545**

and $k_s$ (min$^{-1}$) refer to the first order and second order rate constants, respectively.

## 2.5 *In situ* DRIFTS studies

The *in situ* DRIFTS experiments were performed on a Nicolet iS10 spectrometer equipped with a liquid nitrogen-cooled MCT detector and a diffuse reflectance cell (Harrick Scientific Praying Mantis) with two ZnSe windows and one glass observation window. 20 mg of the powder sample was placed in a porous screen at the bottom of the cell. Then, the cell was quickly sealed and the sample was pretreated in N$_2$ at 120 °C for 3 h. After cooling to room temperature, a background spectrum was firstly measured in N$_2$. Subsequently, when N$_2$ was switched to a gas mixture composed of styrene and air, collection of the DRIFTS spectra was started by averaging 32 scans at a resolution of 4 cm$^{-1}$.

## 2.6 Temperature programmed desorption experiments

To obtain the desorption activation energies of styrene on the UiO-66 and Ag/UiO-66 nanocomposites, temperature-programmed desorption (TPD) experiments were performed. Each sample was activated at 130 °C under vacuum for 10 h. After cooling to room temperature, the sample was instantly transferred into a penicillin bottle containing a given concentration of styrene, and the penicillin bottle was placed in a glovebox overnight. The sample with adsorbed VOCs was transferred to a quartz tube and purged in N$_2$ (40 mL min$^{-1}$ at 40 °C) for 60 min. Subsequently, the heating procedures began, with different heating rates from 3 to 7 K min$^{-1}$, respectively. The effluents were detected by a control system (TP-5076, Xian Quan, China) with temperature coefficients of delay detectors. The desorption activation energies of styrene on the UiO-66 and Ag/UiO-66 samples could be calculated based on their TPD curves. Assuming that the desorption process follows first-order kinetics, the following expression for the desorption activation energy was also obtained based on the Polanyi–Wigner eqn (7):

$$-\ln\left(\frac{\beta_H}{RT_p{}^2}\right) = \frac{E_d}{RT_p} + \ln\left(\frac{E_d}{k_0}\right) \qquad (7)$$

where $E_d$ (kJ mol$^{-1}$) represents the desorption activation energy of styrene on the adsorbate, $\beta_H$ (K min$^{-1}$) refers to the heating rate, and $T_p$ (K) refers to the temperature of the peak in the desorption curve.

# 3. Results and discussion

## 3.1 Material characterization

The XRD patterns of the UiO-66 and Ag/UiO-66 nanocomposites are displayed in Fig. S1.† The characteristic diffraction peaks of the Ag/UiO-66 samples were in accordance with the parent UiO-66, implying that the UiO-66 structure was stable during Ag loading. However, no characteristic peaks correlated with Ag could be observed, probably due to the high dispersion and low loading amount of Ag nanoparticles in the Ag/UiO-66 samples. Additionally, the actual Ag loadings of the Ag/UiO-66 samples measured by AAS were 0.46, 0.89, 1.88 and 2.85 wt% (Table 1), which were very close to their corresponding theoretical loadings. As displayed in Fig. S2,† pure UiO-66 displayed a typical octahedral shape, as observed by TEM. After the loading of Ag nanoparticles on UiO-66, the sizes and morphologies of the parent UiO-66 were still retained well (Fig. 1), demonstrating that the loading of Ag did not change the structure of UiO-66. Moreover, TEM images and the corresponding size distribution histogram as well as the EDX elemental mapping of the Ag/UiO-66 sample visually showed that Ag nanoparticles with sizes of approximately 3–4 nm were unevenly dispersed on UiO-66, and no apparent aggregation was observed regardless of the 3 wt% Ag loading (Fig. 1 and S3†).

It is well known that the specific surface area and pore structure of an adsorbent influence its adsorption–desorption properties.[14,30] Therefore, the textural properties of the synthesized samples were investigated by N$_2$ physisorption measurements at 77 K, and the results are displayed in Fig. 2 and Table 1. The N$_2$ physisorption isotherms of pure UiO-66 and Ag/UiO-66 with different Ag loadings (Fig. 2a) all exhibited typical type I curves due to the presence of micropores. Based on the isotherms of UiO-66, its BET surface area and total pore volume were found to be 1479 m$^2$ g$^{-1}$ and 0.62 cm$^3$ g$^{-1}$ (Table 1), respectively. Comparatively, the Ag/UiO-66 samples displayed slight decreases in both BET surface area and total pore volume after the loading of Ag into UiO-66 (Fig. 2 and Table 1). Moreover, the BET surface area and total pore volume generally decreased as the Ag loading was increased. This can be attributed to partial blockage of the cavities by the well-dispersed Ag nanoparticles and the contributions of non-porous Ag nanoparticles to the total mass of the Ag/UiO-66 composites.

**Table 1** Characterization results of UiO-66 and the Ag/UiO-66 adsorbents

| Sample | $S_{BET}$ (m$^2$ g$^{-1}$) | $S_{Langmuir}$ (m$^2$ g$^{-1}$) | $V_{pore}$ (cm$^3$ g$^{-1}$) | Actual Ag loading (wt%) |
|---|---|---|---|---|
| UiO-66 | 1479 | 1582 | 0.62 | — |
| 0.5 wt% Ag/UiO-66 | 1414 | 1507 | 0.60 | 0.46 |
| 1 wt% Ag/UiO-66 | 1363 | 1461 | 0.59 | 0.89 |
| 2 wt% Ag/UiO-66 | 1288 | 1346 | 0.54 | 1.88 |
| 3 wt% Ag/UiO-66 | 1169 | 1273 | 0.50 | 2.85 |

**546** | *Environ. Sci.: Nano*, 2021, **8**, 543–553
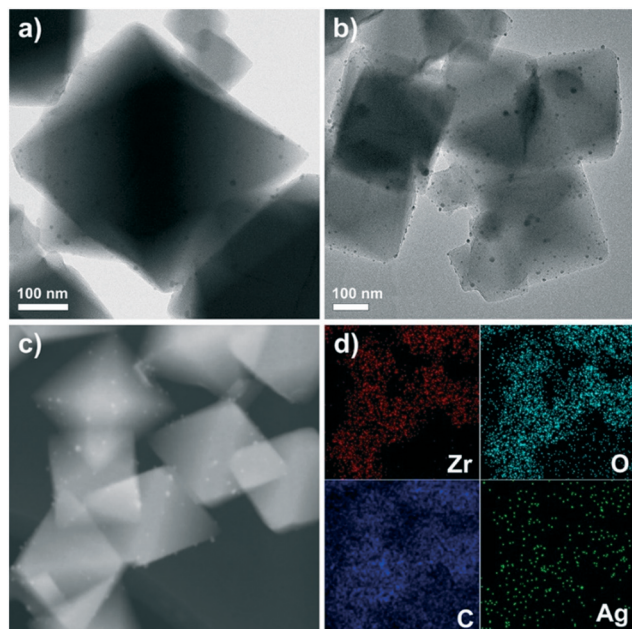
This journal is © The Royal Society of Chemistry 2021

**Fig. 1** TEM images of the Ag/UiO-66 adsorbents with Ag loadings of 2 wt% (a) and 3 wt% (b). HAADF-STEM image (c) of Ag/UiO-66 with Ag loading of 2 wt% and the corresponding EDX elemental mapping (d).
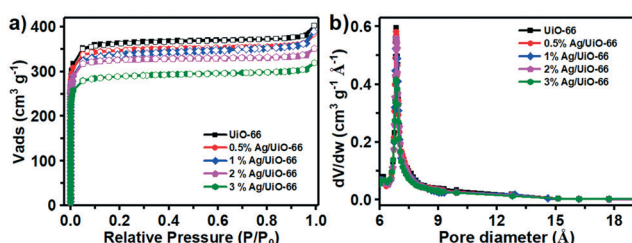


**Fig. 2** N$_2$ adsorption–desorption isotherms (a) and pore-size distribution curves (b) of pure UiO-66 and Ag/UiO-66 with Ag loadings of 0.5, 1, 2 and 3 wt%, respectively.

The optical responses of the UiO-66 and Ag/UiO-66 samples were investigated *via* UV-vis diffuse reflection spectra (Fig. 3a). The pure UiO-66 only showed a strong absorption peak at *ca.* 270 nm. In addition to the similar peak to UiO-66, the Ag/UiO-66 with 0.5 wt% Ag exhibited a new absorption peak at approximately 400 nm resulting from the LSPR excitation of the Ag nanoparticles. Notably, the light absorption intensities were significantly enhanced and the light harvesting range gradually extended to 800 nm as the Ag content was increased. These observations suggest that the optical response of UiO-66 can be effectively regulated by adjusting the content of Ag nanoparticles and that Ag/UiO-66 is an outstanding light absorbing material for potential photothermal conversion.

To better understand the photothermal properties, the pure UiO-66 and Ag/UiO-66 were irradiated by simulated solar light with a wavelength range of 320–780 nm; meanwhile, their surface temperatures were monitored using a thermal imaging infrared camera. When the quartz slide
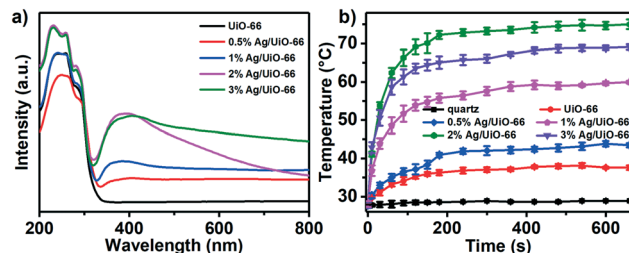


**Fig. 3** UV-vis diffuse reflectance spectra (a) and time-dependent temperature curves under simulated solar light irradiation (b) of pure UiO-66 and the Ag/UiO-66 adsorbents with Ag loadings of 0.5, 1, 2 and 3 wt%, respectively.

was exposed to simulated solar light, the surface temperature was only raised by approximately 1.3 °C after 660 s (Fig. 3b), suggesting that the quartz slide would have a negligible temperature influence on the investigated photothermal materials. Interestingly, the temperature of the 0.5 wt% Ag/UiO-66 was rapidly boosted from 27.8 to 43.9 °C, whereas the temperature increase of pure UiO-66 in a control experiment was only 9.8 °C after 660 s (Fig. 3b). Furthermore, with increasing Ag loading, both the heating rate and stable temperature of Ag/UiO-66 were obviously raised; however, the temperature curves all presented a rapid increase and subsequent plateau. Notably, 2 wt% Ag/UiO-66 exhibited optimal photothermal performance, and the stable temperature reached 75.0 °C within 11 min. However, the temperature was stable at 69.1 °C and lower than that of 2 wt% Ag/UiO-66 when the Ag loading was further increased to 3 wt%, which may be associated with the size and content of Ag on UiO-66.[31]

### 3.2 Adsorption kinetics and photothermal desorption regeneration of adsorbents

**3.2.1 Adsorption kinetics and breakthrough modelling of styrene.** Styrene is an important aromatic chemical that is widely utilized in synthetic rubber, plastics, polyesters and resins, *etc.*[32,33] However, due to its high volatility, styrene is inevitably discharged into the atmosphere and has numerous adverse effects on both humans and ecosystems. Thus, styrene, as a representative VOC, was chosen as a model substrate to evaluate the adsorption and photothermal desorption regeneration performance of the pristine UiO-66 and Ag/UiO-66 nanocomposites. Initially, the adsorption tests were conducted using pristine UiO-66 as an adsorbent under 200 ± 1 ppmv styrene at a flow rate of 25 mL min$^{-1}$. As shown in Fig. 4a, the ratio of the outlet styrene concentration to the inlet styrene concentration immediately dropped to near zero within 2 min and began to emerge until 1910 min with pristine UiO-66. Moreover, the complete breakthrough time could extend to 3230 min and the equilibrium adsorption capacity of styrene on pure UiO-66 was estimated to be 569.4 mg g$^{-1}$ by eqn (3), indicating the outstanding adsorption capacity of UiO-66 for styrene. After the loading of Ag on UiO-66, the breakthrough curves were similar to those
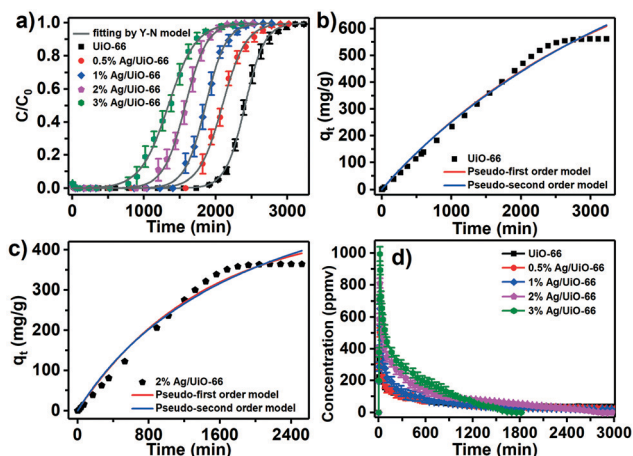
This journal is © The Royal Society of Chemistry 2021

*Environ. Sci.: Nano*, 2021, **8**, 543–553 | **547**

**Fig. 4** The breakthrough curves (symbols) and corresponding fitting curves by the Yoon–Nelson model (solid line) of pure UiO-66 and the Ag/UiO-66 adsorbents with Ag loadings of 0.5, 1, 2 and 3 wt%, respectively (a); experimental styrene uptake and corresponding fitting curves from the pseudo-first order kinetic model and second order kinetic model of pure UiO-66 (b) and the Ag/UiO-66 adsorbent with Ag loading of 2 wt% (c); and the corresponding desorption curves under the irradiation of a 300 W Xe lamp (d).

of pristine UiO-66. However, the breakthrough times gradually decreased as the Ag loading content increased, and the adsorption amounts of styrene on Ag/UiO-66 with Ag loadings of 0.5, 1, 2 and 3 wt% were obtained as 489.1, 432.5, 364.6 and 323.6 mg g$^{-1}$ (Table S1†), respectively, implying a decreasing adsorption capacity with increasing Ag loading content. It is known that the specific surface areas and the pore structures of adsorbents influence their adsorption properties.[14,30,34] As shown in Fig. 2 and Table 1, the specific surface areas were in the order of UiO-66 > 0.5 wt% Ag/UiO-66 > 1 wt% Ag/UiO-66 > 2 wt% Ag/UiO-66 > 3 wt% Ag/UiO-66, which was obviously consistent with the order of their adsorption amounts. Furthermore, considering that the loading of Ag on UiO-66 did not alter the pore size of UiO-66, it is reasonable to speculate that the decreased adsorption capacities of Ag/UiO-66 were closely correlated with their declined specific surface areas compared with those of UiO-66.

Additionally, the styrene dynamic adsorption behaviours were predicted by the Yoon–Nelson model according to the following eqn (8):[35]

$$t = \tau + \frac{1}{k}\text{ln}\left(\frac{C_t}{C_0 - C_t}\right) \tag{8}$$

where $C_0$ (mg L$^{-1}$) refers to the inlet concentration of styrene, $C_t$ (mg L$^{-1}$) refers to the effluent concentration of styrene at breakthrough time $t$ (min), $\tau$ (min) represents the time taken to reach 50% breakthrough of styrene, and $k$ is the kinetic constant based on the styrene diffusion characteristic in the fixed bed reactor.

As can be seen in Fig. 4a, the predicted breakthrough curves of the Yoon–Nelson model can simulate the experimental breakthrough data well, with regression

**Table 2** Fitting parameters for breakthrough curves by a Yoon–Nelson model

| Sample | $\tau$ (min) | $k$ (min$^{-1}$) | $R^2$ |
|---|---|---|---|
| UiO-66 | 2408.47 | 0.00737 | 0.999 |
| 0.5 wt% Ag/UiO-66 | 2091.62 | 0.00612 | 0.998 |
| 1 wt% Ag/UiO-66 | 1857.45 | 0.00699 | 0.999 |
| 2 wt% Ag/UiO-66 | 1574.99 | 0.00663 | 0.999 |
| 3 wt% Ag/UiO-66 | 1337.82 | 0.00517 | 0.998 |

coefficients of $R^2 > 0.99$ for all the investigated adsorbents (Table 2). The fitting parameters listed in Table 2 display that the rate constant $k$ and fitted time $\tau$ for styrene adsorption on UiO-66 are both larger than that of Ag/UiO-66. Moreover, the fitted time $\tau$ declined gradually with increasing Ag loading amount, indicating that the loading of Ag on UiO-66 could affect both the adsorption kinetics and capacity. However, the trends of these fitting parameters observed in the predicted breakthrough curves were well matched with those in the experimental breakthrough curves.

A pseudo-first order model and pseudo-second order model were employed to analyse the adsorption kinetics of styrene on UiO-66 and Ag/UiO-66 based on their breakthrough curves. The experimental adsorption amounts of styrene (points) and the theoretical curves (lines) are presented in Fig. 4b and c and S4–S6.† In addition, the kinetic parameters estimated for both the models and the correlation coefficients of $R^2$ are summarized in Table 3. The kinetics constant $k_f$ and $k_s$ increased as the Ag content on UiO-66 increased regardless of the kinetic model that was used (Table 3). However, a lower adsorption amount of styrene was predicted with increasing Ag loading despite its faster adsorption rate, which would be relevant to the shortened diffusion distance of styrene through the partial blockage of pores in UiO-66 by the loaded Ag nanoparticles. As can be seen in Fig. 4b and c and S4–S6,† both the pseudo-first order model and pseudo-second order model can follow the initial stages of adsorption. However, when the adsorption equilibrium was approached, the adsorption amounts were obviously overestimated by the pseudo-second order model for all the investigated adsorbents. The $R^2$ values of the pseudo-first order model were in the range of 0.989–0.990, which were higher than that of the corresponding pseudo-second order model (0.984–0.989). Furthermore, it is clear from the comparison of the predicted and experimental adsorption amounts that the equilibrium adsorption amounts obtained by the pseudo-first order model were more approximate to the experimental values. The above results revealed that the pseudo-first order model could better describe the adsorption behaviours than the pseudo-second order model. It is well accepted that the pseudo-first order model is suitable to predict the adsorption behaviours based on physical interactions, while the pseudo-second order model is proposed on the basis of a strong chemical interaction between the adsorbate and adsorbent.[8,36] Therefore, it is plausible that physical adsorption by

**548** | *Environ. Sci.: Nano*, 2021, **8**, 543–553

This journal is © The Royal Society of Chemistry 2021

**Table 3**  Coefficients of the kinetic equations for the adsorption of styrene on the adsorbents

| Sample | Pseudo-first-order | | | Pseudo-second-order | | |
|---|---|---|---|---|---|---|
| | $q_e$ (mg g$^{-1}$) | $k_f$ ($10^{-4}$ min$^{-1}$) | $R^2$ | $q_e$ (mg g$^{-1}$) | $k_s$ ($10^{-4}$ min$^{-1}$) | $R^2$ |
| UiO-66 | 997 | 2.92 | 0.990 | 1724 | 0.99 | 0.989 |
| 0.5 wt% Ag/UiO-66 | 714 | 4.42 | 0.990 | 1159 | 2.42 | 0.989 |
| 1 wt% Ag/UiO-66 | 598 | 5.43 | 0.989 | 952 | 3.71 | 0.987 |
| 2 wt% Ag/UiO-66 | 468 | 7.18 | 0.989 | 719 | 6.83 | 0.986 |
| 3 wt% Ag/UiO-66 | 365 | 9.48 | 0.989 | 528 | 13.60 | 0.984 |

micropore volume filling is a predominant mechanism for UiO-66 and Ag/UiO-66. This conclusion was also supported by the close correlations between the equilibrium styrene adsorption capacities of UiO-66 and Ag/UiO-66 and their specific surface areas (Fig. 2 and Table 1).

**3.2.2 Photothermal regeneration of adsorbents.** After the adsorption equilibrium was accomplished, the *in situ* photothermal desorption test was also performed under Xe lamp irradiation, and the results are shown in Fig. 4d. It was clearly observed that a roll-up phenomenon appeared in all the desorption curves regardless of the Ag loading, which would be relevant to their excellent equilibrium adsorption capacity. When the lamp was turned on, plentiful adsorbed styrene would be released from the surface of adsorbents due to their high adsorption capacities, thus leading to high outlet concentration within the initial degradation stage. For the pure UiO-66, the outlet styrene concentration rapidly ascended to its highest point of 332.9 ppmv within the initial 10 min and then gradually decreased. When 0.5 wt% Ag was introduced into UiO-66, the highest point of the outlet styrene concentration was boosted to 503.3 ppmv. Moreover, the highest point of the outlet styrene concentration was raised with increasing Ag loading despite the lower equilibrium adsorption capacity. More importantly, the adsorbed styrene on Ag/UiO-66 with Ag loadings of 2 and 3 wt% could be almost completely desorbed after 2800 and 1815 min of irradiation, respectively. However, it was difficult to achieve complete desorption of styrene on UiO-66 because the desorption rate was very sluggish after long irradiation. For instance, the styrene desorption capacity was only improved from 158.7 to 207.2 mg g$^{-1}$ with the increase of the irradiation time from 2005 to 3145 min. For the Ag/UiO-66 samples with Ag loadings of 0.5 and 1 wt%, their styrene desorption capacities were 198.8 and 219.4 mg g$^{-1}$ after around 3000 min of irradiation. Given that the desorption rates of all the investigated adsorbents noticeably slowed with the irradiation time, we also compared their styrene desorption capacities within 875 min of irradiation. As displayed in Table S1,† the styrene desorption efficiency of pure UiO-66 was only 18.1% after 875 min of irradiation, whereas 0.5 wt% Ag/UiO-66 could offer 22.3% desorption efficiency under the same conditions. Remarkably, the styrene desorption efficiency was also distinctly improved from 22.3% to 85.3% as the Ag loading content was raised from 0.5 to 3.0 wt%. Meanwhile, the generated $CO_2$ amounts during the irradiation process were measured. The results

displayed that no $CO_2$ was detected in the presence of pure UiO-66 and Ag/UiO-66 during the irradiation processes, implying that the mineralization could be negligible under the investigated conditions. Furthermore, we investigated the styrene desorption performance on pure UiO-66 at 75 °C. The results showed that the styrene adsorbed on UiO-66 could be completely desorbed after heating for 2500 min (Fig. S7†). These results disclosed that the Ag nanoparticles were indispensable partners to release the adsorbed styrene from the adsorbent, and the *in situ* regeneration of Ag/UiO-66 can be facilely achieved under light irradiation.

Reusability is a crucial factor for an adsorbent, and it usually determines the potentiality of the adsorbent for practical application. Therefore, five runs of *in situ* adsorption–desorption were performed using pure UiO-66 and 2 wt% Ag/UiO-66 as adsorbents. After each adsorption equilibrium, a 300 W Xe lamp irradiated the adsorbent to desorb the adsorbed styrene prior to the following adsorption run. In the presence of 2.0 wt% Ag/UiO-66, both the adsorption and desorption curves during the five adsorption–desorption cycles were very consistent with that in the first run (Fig. 5a). Furthermore, the adsorption capacities estimated from their breakthrough curves were in the range of 359.7–368.2 mg g$^{-1}$, and the desorption capacities were maintained at 342.8–350.0 mg g$^{-1}$ during the five successive runs. These results obviously reveal that there was hardly any diminution in either the adsorption capacity or desorption
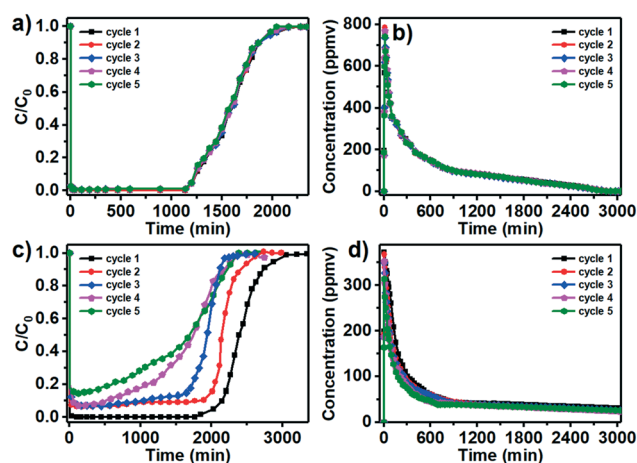


**Fig. 5** Cycle performance of styrene adsorption and desorption on the 2 wt% UiO-66 (a and b) and pure UiO-66 (c and d) adsorbents.

capacity in the presence of 2.0 wt% Ag/UiO-66 (Fig. 5a and b). Considering the very slow styrene desorption rate of UiO-66 after long irradiation, 3000 min of irradiation was chosen for each desorption. The styrene adsorption capacities of UiO-66 during the five runs were 561.7, 449.3, 407.1, 328.9 and 290.2 mg g$^{-1}$, respectively. In sharp contrast, only 51.6% of the adsorption capacity was retained after the fifth run of adsorption–desorption using pure UiO-66 as the adsorbent (Fig. 5c). Additionally, the styrene concentration during the desorption process decreased with increasing adsorption–desorption cycle number, and the desorption capacity showed a gradual decrease from 212.9 mg g$^{-1}$ in the first run to 163.9 mg g$^{-1}$ in the fifth run (Fig. 5d). The above results demonstrate that the modification of UiO-66 with Ag nanoparticles could substantially improve its photo-induced VOC desorption performance, thus resulting in extraordinary regenerability of Ag/UiO-66 under solar light irradiation.

### 3.3 Regeneration mechanism of the adsorbents

*In situ* DRIFTS experiments were performed to obtain insight into the difference in styrene adsorption on the pure UiO-66 and Ag/UiO-66 at the molecular level. Initially, the adsorption of gaseous styrene on Ag/UiO-66 was investigated, and the results are displayed in Fig. 6. The results showed bands at 3080 and 3060 cm$^{-1}$, which can be attributed to the stretching vibration of aromatic C–H bonds.[37,38] The band at 1510 cm$^{-1}$ was related to the skeleton vibrations of the benzene ring in the UiO-66 structure.[37,38] Two very strong bands observed at around 1600 and 1450 cm$^{-1}$ were correlated with the asymmetric and symmetric stretching vibrations of COO$^{-}$.[39,40] After the introduction of styrene, five new absorption bands, including the C–H stretching vibration of alkenes at 3025 and 3010 cm$^{-1}$, the C–H bending

vibration at 990 and 910 cm$^{-1}$, and the aromatic C–H bending vibration at 780 cm$^{-1}$, appeared, and their intensities were enhanced with prolonged adsorption time, indicating that styrene was gradually adsorbed onto 2.0 wt% Ag/UiO-66 (Fig. 6 and S8†). Meanwhile, the stretching vibrations of COO$^{-}$ at 1600 and 1450 cm$^{-1}$ as well as the skeleton vibrations of the benzene ring at 1510 cm$^{-1}$ within the UiO-66 structure became weaker and showed slight red shifts as the adsorption time was increased, which can be attributed to the increased electron density of the Zr sites.[41,42] In addition, the peak at 3674 cm$^{-1}$ assigned to the terminal-OH groups on the Zr-node of the UiO-66 framework decreased gradually, while the hydroxyl peak of bound water was formed at 3589 cm$^{-1}$.[40]

To further verify the potential adsorption by the interactions between the Lewis basic alkene C=C bonds in styrene with the Lewis acidic sites on the surface of UiO-66 and Ag/UiO-66 absorbents, the surface acidity of the prepared samples was investigated using a pyridine adsorption method. The results included in Fig. S9 and Table S2† demonstrated that the parent UiO-66 possessed a high total acidity of 227.2 μmol g$^{-1}$ comprised of Lewis acidity of 193.6 μmol g$^{-1}$ and Brønsted acidity of 33.6 μmol g$^{-1}$. The Lewis acidity would derive from the coordinatively unsaturated Zr sites after the terminal H$_2$O elimination within the UiO-66. However, the surface Lewis acidity of Ag/UiO-66 revealed a slight reduction compared to that of pure UiO-66, while the Brønsted acidity remained unchanged. Considering the presence of Zr Lewis acids on UiO-66, it can be speculated that styrene was adsorbed on the Zr Lewis acid sites of UiO-66 by the electron-rich C=C bonds of alkenes in addition to micropore volume filling, thus gradually replacing the terminal-OH adsorbed on the Zr Lewis acids. Moreover, the electron donation effect of the C=C bond of the alkene to its adsorbed Zr site may increase the electron density of the Zr sites, which was responsible for the variations of the COO$^{-}$ groups coordinated with Zr within UiO-66. Compared to Ag/UiO-66, the characteristic peaks and observed variations in pristine UiO-66 before and after the introduction of styrene were almost consistent with those of Ag/UiO-66 (Fig. 6 and S10†), suggesting that the loading of Ag nanoparticles on UiO-66 would not change the adsorption behaviours of styrene.

For an adsorbent, the desorption activation energy is essential to obtain a fundamental understanding of its regenerability. In view of this, a series of TPD experiments were also performed at heating rates from 3 to 7 K min$^{-1}$ to estimate the desorption activation energies of styrene on pristine UiO-66 and the Ag/UiO-66 nanocomposites with different Ag loadings. As presented in Fig. 7, only one peak was observed in each TPD curve of styrene desorbed from the investigated adsorbents, suggesting that there is one major site in UiO-66 and Ag/UiO-66 for styrene adsorption. Evidently, the temperature of the peak on the desorption curve of pristine UiO-66 was higher than that on the Ag/UiO-66 nanocomposites. It was also noted that the temperature of
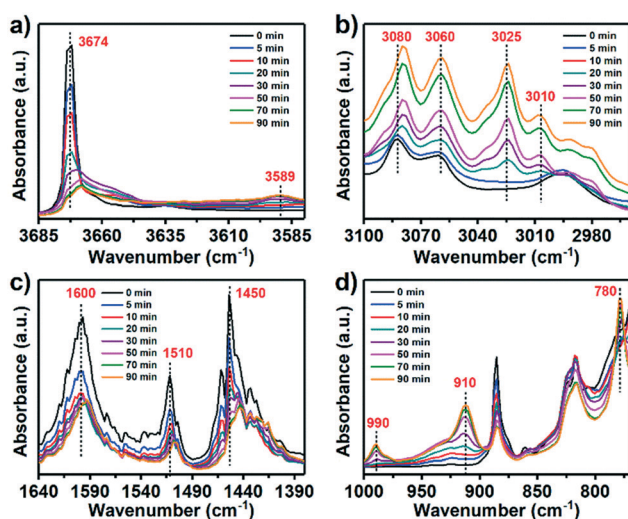


**Fig. 6** *In situ* DRIFTS spectra of 2 wt% Ag/UiO-66 in the range of 3685–3580 cm$^{-1}$ (a), 3100–2960 cm$^{-1}$ (b), 1640–1380 cm$^{-1}$ (c) and 1000–770 cm$^{-1}$ (d) during styrene adsorption at different times in the range of 0–90 min.

**550** | *Environ. Sci.: Nano*, 2021, **8**, 543–553

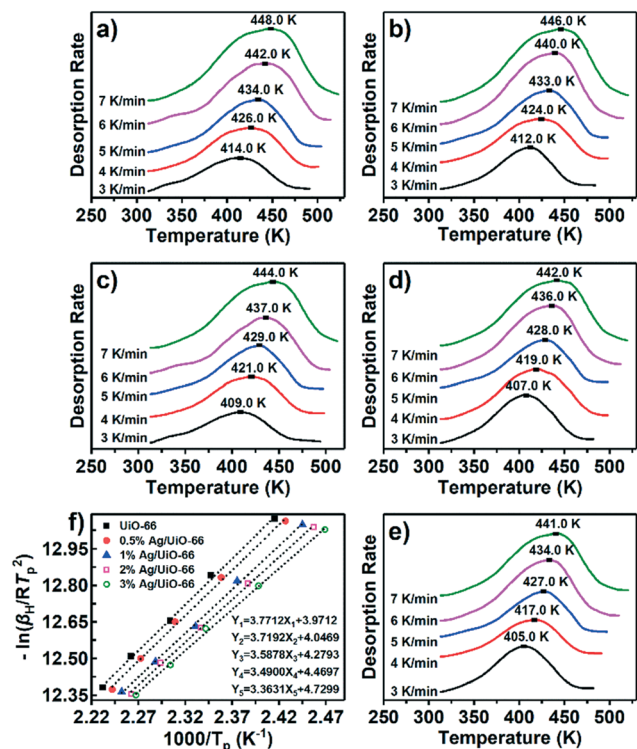This journal is © The Royal Society of Chemistry 2021

**Fig. 7** TPD spectra of styrene on pure UiO-66 (a); Ag/UiO-66 adsorbents with Ag loadings of 0.5 (b), 1 (c), 2 (d) and 3 (e) wt%, respectively, at different heating rates in the range of 3–7 K min$^{-1}$ (N$_2$ flow rate = 40 mL min$^{-1}$). The corresponding linear dependence between $\ln[\beta_H/RT_p^2]$ and $1/T_p$ derived from TPD results of styrene on the UiO-66 and Ag/UiO-66 adsorbents (f).

the peak gradually decreased as the Ag loading increased at the same investigated conditions. These results demonstrated that it is less difficult to release styrene from Ag/UiO-66 with increased Ag loading. Based on eqn (7), the desorption activation energies of Ag/UiO-66 with 0.5, 1.0, 2.0 and 3.0 wt% were estimated to be 30.9, 29.8, 29.0 and 28.0 kJ mol$^{-1}$, respectively, which were lower than that of pristine UiO-66 (31.4 kJ mol$^{-1}$, Table S3†). Considering that physical interaction was principally involved during the adsorption of styrene on pristine UiO-66 and Ag/UiO-66, the partial blockage of the pores in UiO-66 by Ag nanoparticles would render a moiety of the pores useless and thus shorten the diffusion length of styrene in the pore channels, which would be responsible for their decreased desorption activation energy.

On the basis of the above results, a plausible mechanism for the regeneration of Ag/UiO-66 was tentatively proposed. A careful comparison of the pristine UiO-66 and Ag/UiO-66 revealed that the introduction of a small amount of Ag nanoparticles caused almost no change in the adsorption mechanism and slightly affected the desorption activation energy. However, the styrene desorption capabilities of the Ag/UiO-66 nanocomposites were improved significantly. Therefore, it is speculated that the excellent photothermal properties of the Ag nanoparticles is responsible for their

superior regenerability. First, due to the plentiful interconnected 3D cavities of Ag/UiO-66 accessible with the open pores of UiO-66, it exhibited excellent adsorption capacity of styrene, which would give rise to a high local concentration of styrene to surround the highly dispersed Ag nanoparticles. Second, heat was produced on the surfaces of the Ag nanoparticles, induced by their outstanding SPR response, when the Ag/UiO-66 composites were irradiated by the simulated solar light (Fig. 3b). Owing to the inherent inferior thermal conductivity of MOFs,[43] the heat transfer and heat loss would be effectively suppressed and thus give rise to localized light induction heat near the Ag nanoparticles. Subsequently, this localized heat might be transported to both the surrounding UiO-66 and the high concentration of adsorbed styrene, eventually triggering and accelerating the desorption of styrene from the surface of the Ag/UiO-66 adsorbent. As a result, outstanding photo-induced regeneration capability of the Ag/UiO-66 adsorbent was achieved under the simulated solar light irradiation.

## Conclusions

In summary, a photothermally induced renewable adsorbent, Ag/UiO-66 nanocomposite, was successfully constructed by loading of Ag nanoparticles on UiO-66 through a facile colloidal deposition method. The obtained Ag/UiO-66 samples were found to retain the regular morphology and excellent porosity as well as the outstanding styrene adsorption capability of the parent UiO-66. Upon exposure to simulated solar light, the temperature of the Ag/UiO-66 samples could be instantly elevated, and the 2.0 wt% Ag/UiO-66 exhibited optimal photothermal performance with a temperature increase of 47.2 °C. This localized heat was able to trigger the desorption of the adsorbed styrene from Ag/UiO-66, thus successfully realizing efficient *in situ* regeneration of the adsorbent under solar light irradiation. Impressively, no appreciable decline was observed in either the adsorption or desorption efficiencies for 2.0 wt% Ag/UiO-66 even after five adsorption and desorption cycles; however, only 51.6% of the styrene adsorption capacity and 77.0% of the desorption capacity were maintained after five runs in the presence of pristine UiO-66. Considering the exceptional adsorption properties and green *in situ* regeneration process triggered by naturally abundant solar light, we speculate that the development of photothermal MOF-based composites will open new avenues for exploiting novel adsorbents.

## Conflicts of interest

There are no conflicts to declare.

## Acknowledgements

This journal is © The Royal Society of Chemistry 2021

*Environ. Sci.: Nano*, 2021, **8**, 543–553 | **551**

## Notes and references

1 C. He, J. Cheng, X. Zhang, M. Douthwaite, S. Pattisson and Z. P. Hao, Recent advances in the catalytic oxidation of volatile organic compounds: A review based on pollutant sorts and sources, *Chem. Rev.*, 2019, **119**, 4471–4568.

2 Y. Ji, Q. Shi, Y. Li, T. An, J. Zheng, J. Peng, Y. Gao, J. Chen, G. Li, Y. Wang, F. Zhang, A. L. Zhang, J. Zhao, M. J. Molina and R. Zhang, Carbenium ion-mediated oligomerization of methylglyoxal for secondary organic aerosol formation, *Proc. Natl. Acad. Sci. U. S. A.*, 2020, **117**, 13294–13299.

3 A. Mellouki, T. J. Wallington and J. Chen, Atmospheric chemistry of oxygenated volatile organic compounds: impacts on air quality and climate, *Chem. Rev.*, 2015, **115**, 3984–4014.

4 X. Ding, H. Liu, J. Chen, M. Wen, G. Li, T. An and H. Zhao, In situ growth of well-aligned Ni-MOF nanosheets on nickel foam for enhanced photocatalytic degradation of typical volatile organic compounds, *Nanoscale*, 2020, **12**, 9462–9470.

5 H. Liu, Y. Ma, J. Chen, M. Wen, G. Li and T. An, Highly efficient visible-light-driven photocatalytic degradation of VOCs by $CO_2$-assisted synthesized mesoporous carbon confined mixed-phase $TiO_2$ nanocomposites derived from MOFs, *Appl. Catal., B*, 2019, **250**, 337–346.

6 C. H. A. Tsang, K. Li, Y. Zeng, W. Zhao, T. Zhang, Y. Zhan, R. Xie, D. Y. C. Leung and H. Huang, Titanium oxide based photocatalytic materials development and their role of in the air pollutants degradation: Overview and forecast, *Environ. Int.*, 2019, **125**, 200–228.

7 Y. L. Wang, Z. H. Li, C. Tang, H. X. Ren, Q. Zhang, M. Xue, J. Xiong, D. B. Wang, Q. Yu, Z. Y. He, F. Wei and J. K. Jiang, Few-layered mesoporous graphene for high-performance toluene adsorption and regeneration, *Environ. Sci.: Nano*, 2019, **6**, 3113–3122.

8 X. Zhang, B. Gao, J. Fang, W. Zou, L. Dong, C. Cao, J. Zhang, Y. Li and H. Wang, Chemically activated hydrochar as an effective adsorbent for volatile organic compounds (VOCs), *Chemosphere*, 2019, **218**, 680–686.

9 C. T. Yang, G. Miao, Y. H. Pi, Q. B. Xia, J. L. Wu, Z. Li and J. Xiao, Abatement of various types of VOCs by adsorption/catalytic oxidation: A review, *Chem. Eng. J.*, 2019, **370**, 1128–1153.

10 X. Zhang, B. Gao, A. E. Creamer, C. Cao and Y. Li, Adsorption of VOCs onto engineered carbon materials: A review, *J. Hazard. Mater.*, 2017, **338**, 102–123.

11 K. Vellingiri, P. Kumar and K.-H. Kim, Coordination polymers: Challenges and future scenarios for capture and degradation of volatile organic compounds, *Nano Res.*, 2016, **9**, 3181–3208.

12 S. W. Nahm, W. G. Shim, Y.-K. Park and S. C. Kim, Thermal and chemical regeneration of spent activated carbon and its adsorption property for toluene, *Chem. Eng. J.*, 2012, **210**, 500–509.

13 L. Y. Chen, R. Luque and Y. W. Li, Controllable design of tunable nanostructures inside metal-organic frameworks, *Chem. Soc. Rev.*, 2017, **46**, 4614–4630.

14 M. Wen, G. Li, H. Liu, J. Chen, T. An and H. Yamashita, Metal-organic framework-based nanomaterials for adsorption and photocatalytic degradation of gaseous pollutants: recent progress and challenges, *Environ. Sci.: Nano*, 2019, **6**, 1006–1025.

15 Z. Y. Zhou, B. H. Cheng, C. Ma, F. Xu, J. Xiao, Q. B. Xia and Z. Li, Flexible and mechanically-stable MIL-101(Cr)@PFs for efficient benzene vapor and $CO_2$ adsorption, *RSC Adv.*, 2015, **5**, 94276–94282.

16 P. Kumar, K. H. Kim, E. E. Kwon and J. E. Szulejko, Metal-organic frameworks for the control and management of air quality: advances and future direction, *J. Mater. Chem. A*, 2016, **4**, 345–361.

17 K. Vellingiri, P. Kumar, A. Deep and K. H. Kim, Metal-organic frameworks for the adsorption of gaseous toluene under ambient temperature and pressure, *Chem. Eng. J.*, 2017, **307**, 1116–1126.

18 X. Q. Li, L. Zhang, Z. Q. Yang, P. Wang, Y. F. Yan and J. Y. Ran, Adsorption materials for volatile organic compounds (VOCs) and the key factors for VOCs adsorption process: A review, *Sep. Purif. Technol.*, 2020, **235**, 116213–116228.

19 X. J. Sun, Q. B. Xia, Z. X. Zhao, Y. W. Li and Z. Li, Synthesis and adsorption performance of MIL-101(Cr)/graphite oxide composites with high capacities of n-hexane, *Chem. Eng. J.*, 2014, **239**, 226–232.

20 X. Zhang, Y. Yang, X. Lv, Y. Wang, N. Liu, D. Chen and L. Cui, Adsorption/desorption kinetics and breakthrough of gaseous toluene for modified microporous-mesoporous UiO-66 metal organic framework, *J. Hazard. Mater.*, 2019, **366**, 140–150.

21 M. Shafiei, M. S. Alivand, A. Rashidi, A. Samimi and D. Mohebbi-Kalhori, Synthesis and adsorption performance of a modified micro-mesoporous MIL-101(Cr) for VOCs removal at ambient conditions, *Chem. Eng. J.*, 2018, **341**, 164–174.

22 J. Chen, J. Feng, Z. Li, P. Xu, X. Wang, W. Yin, M. Wang, X. Ge and Y. Yin, Space-confined seeded growth of black silver nanostructures for solar steam generation, *Nano Lett.*, 2019, **19**, 400–407.

23 J. Guo, Y. Zhang, L. Shi, Y. Zhu, M. F. Mideksa, K. Hou, W. Zhao, D. Wang, M. Zhao, X. Zhang, J. Lv, J. Zhang, X. Wang and Z. Tang, Boosting hot electrons in hetero-superstructures for plasmon-enhanced catalysis, *J. Am. Chem. Soc.*, 2017, **139**, 17964–17972.

24 H. Yang, L. Q. He, Y. W. Hu, X. Lu, G. R. Li, B. Liu, B. Ren, Y. Tong and P. P. Fang, Quantitative detection of photothermal and photoelectrocatalytic effects induced by SPR from Au@Pt nanoparticles, *Angew. Chem., Int. Ed.*, 2015, **54**, 11462–11466.

**552** | *Environ. Sci.: Nano*, 2021, **8**, 543–553

This journal is © The Royal Society of Chemistry 2021

25   S. Kim, J. M. Kim, J. E. Park and J. M. Nam, Nonnoble-metal-based plasmonic nanomaterials: recent advances and future perspectives, *Adv. Mater.*, 2018, **30**, e1704528.

26   C. Kuppe, K. R. Rusimova, L. Ohnoutek, D. Slavov and V. K. Valev, "Hot" in plasmonics: temperature-related concepts and applications of metal nanostructures, *Adv. Opt. Mater.*, 2019, **8**, 1901166.

27   K. Khaletskaya, J. Reboul, M. Meilikhov, M. Nakahama, S. Diring, M. Tsujimoto, S. Isoda, F. Kim, K. I. Kamei, R. A. Fischer, S. Kitagawa and S. Furukawa, Integration of porous coordination polymers and gold nanorods into core-shell mesoscopic composites toward light-induced molecular release, *J. Am. Chem. Soc.*, 2013, **135**, 10998–11005.

28   J. H. Cavka, S. Jakobsen, U. Olsbye, N. Guillou, C. Lamberti, S. Bordiga and K. P. Lillerud, A new zirconium inorganic building brick forming metal organic frameworks with exceptional stability, *J. Am. Chem. Soc.*, 2008, **130**, 13850–13851.

29   C. A. Emeis, Determination of integrated molar extinction coefficients for infrared absorption bands of pyridine adsorbed on solid acid catalysts, *J. Catal.*, 1993, **141**, 347–354.

30   H. Wang and J. Li, Microporous metal-organic frameworks for adsorptive separation of C5-C6 alkane isomers, *Acc. Chem. Res.*, 2019, **52**, 1968–1978.

31   H. Chen, L. Shao, T. Ming, Z. Sun, C. Zhao, B. Yang and J. Wang, Understanding the photothermal conversion efficiency of gold nanocrystals, *Small*, 2010, **6**, 2272–2280.

32   H. Plaisance, J. Vignau-Laulhere, P. Mocho, N. Sauvat, K. Raulin and V. Desauziers, Volatile organic compounds concentrations during the construction process in newly-built timber-frame houses: source identification and emission kinetics, *Environ. Sci.: Processes Impacts*, 2017, **19**, 696–710.

33   Z. Zhang, J. Chen, Y. Gao, Z. Ao, G. Li, T. An, Y. Hu and Y. Li, A coupled technique to eliminate overall nonpolar and polar volatile organic compounds from paint production industry, *J. Cleaner Prod.*, 2018, **185**, 266–274.

34   K. Yang and B. Xing, Adsorption of organic compounds by carbon nanomaterials in aqueous phase: Polanyi theory and its application, *Chem. Rev.*, 2010, **110**, 5989–6008.

35   Y. H. Yoon and J. H. Nelson, Application of gas adsorption kinetics–II. A theoretical model for respirator cartridge service life and its practical applications, *Am. Ind. Hyg. Assoc. J.*, 1984, **45**, 517–524.

36   R. Serna-Guerrero and A. Sayari, Modeling adsorption of $CO_2$ on amine-functionalized mesoporous silica. 2: Kinetics and breakthrough curves, *Chem. Eng. J.*, 2010, **161**, 182–190.

37   J. Liu, Y. Xu, P. B. Groszewicz, M. Brodrecht, C. Fasel, K. Hofmann, X. Tan, T. Gutmann and G. Buntkowsky, Novel dirhodium coordination polymers: the impact of side chains on cyclopropanation, *Catal. Sci. Technol.*, 2018, **8**, 5190–5200.

38   P. Shafieyoon, E. Mehdipour and Y. S. Mary, Synthesis, characterization and biological investigation of glycine-based sulfonamide derivative and its complex: Vibration assignment, HOMO-LUMO analysis, MEP and molecular docking, *J. Mol. Struct.*, 2019, **1181**, 244–252.

39   Y. Han, M. Liu, K. Li, Y. Zuo, Y. Wei, S. Xu, G. Zhang, C. Song, Z. Zhang and X. Guo, Facile synthesis of morphology and size-controlled zirconium metal–organic framework UiO-66: the role of hydrofluoric acid in crystallization, *CrystEngComm*, 2015, **17**, 6434–6440.

40   C. F. Pereira, A. J. Howarth, N. A. Vermeulen, F. A. A. Paz, J. P. C. Tomé, J. T. Hupp and O. K. Farha, Towards hydroxamic acid linked zirconium metal–organic frameworks, *Mater. Chem. Front.*, 2017, **1**, 1194–1199.

41   Sonal, K. K. Pant and S. Upadhyayula, An insight into the promotional effect on Fe-Co bimetallic catalyst in the Fischer Tropsch reaction: A DRIFTS study, *Fuel*, 2020, **276**, 118044.

42   G. Cheng, X. Liu, X. Song, X. Chen, W. Dai, R. Yuan and X. Fu, Visible-light-driven deep oxidation of NO over Fe doped $TiO_2$ catalyst: Synergic effect of Fe and oxygen vacancies, *Appl. Catal., B*, 2020, **277**, 119196.

43   H. Li and M. R. Hill, Low-energy $CO_2$ release from metal-organic frameworks triggered by external stimuli, *Chem. Soc. Rev.*, 2017, **50**, 778–786.

This journal is © The Royal Society of Chemistry 2021

*Environ. Sci.: Nano*, 2021, **8**, 543–553 | **553**